





A linear response framework for simulating bosonic and fermionic correlation functions illustrated on quantum computers

Efehan Kökcü ¹, Heba A. Labib ¹, J. K. Freericks ² and A. F. Kemper ^{1,*}

¹*Department of Physics, North Carolina State University, Raleigh, North Carolina 27695, USA*

²*Department of Physics, Georgetown University, 37th and O Sts. NW, Washington, DC 20057 USA*

(Dated: February 22, 2023)

Response functions are a fundamental aspect of physics; they represent the link between experimental observations and the underlying quantum many-body state. However, this link is often under-appreciated, as the Lehmann formalism for obtaining response functions in linear response has no direct link to experiment. Within the context of quantum computing, and by using a linear response framework, we restore this link by making the experiment an inextricable part of the quantum simulation. This method can be frequency- and momentum-selective, avoids limitations on operators that can be directly measured, and is ancilla-free. As prototypical examples of response functions, we demonstrate that both bosonic and fermionic Green's functions can be obtained, and apply these ideas to the study of a charge-density-wave material on *ibm_auckland*. The linear response method provides a robust framework for using quantum computers to study systems in physics and chemistry. It also provides new paradigms for computing response functions on classical computers.

INTRODUCTION

Quantum computers are showing promise as quantum simulators of many-body physics, with the hope of being able to further our understanding of complex interacting systems. In order to realize this promise, a key task is to compute response functions for a prepared many-body state. They represent the experimental measurements that are performed on the physical realizations of such systems, and computing them via simulation is a critical step in connecting to experiments and building an understanding of the physics they contain. Examples of experiments that measure response functions are neutron scattering, optical spectroscopy, and angle-resolved photoemission spectroscopy (ARPES), which measure the spin-spin correlation, current-current correlation, and single-particle Green's function, respectively[1, 2]. The first two are bosonic correlation functions, while the latter is a fermionic correlation function. Both of these contain valuable information — both have direct links to experiments, and in addition the electronic Green's function is a key ingredient in hybrid-classical algorithms such as dynamical mean field theory[3–8].

There are several techniques for computing correlation functions on quantum computers. The primary tool is based on Hadamard test circuits[9–15]; alternatives include variational approaches[16–20], spectral decomposition[21–23], and linear systems of equation solvers[24]. Each of these has their own advantages and disadvantages, based on the particular quantum algorithms and hardware at hand. For example, one of the challenges with the Hadamard test is the need to maintain coherence between the ancilla and the system for the potentially long length of time in the measured correla-

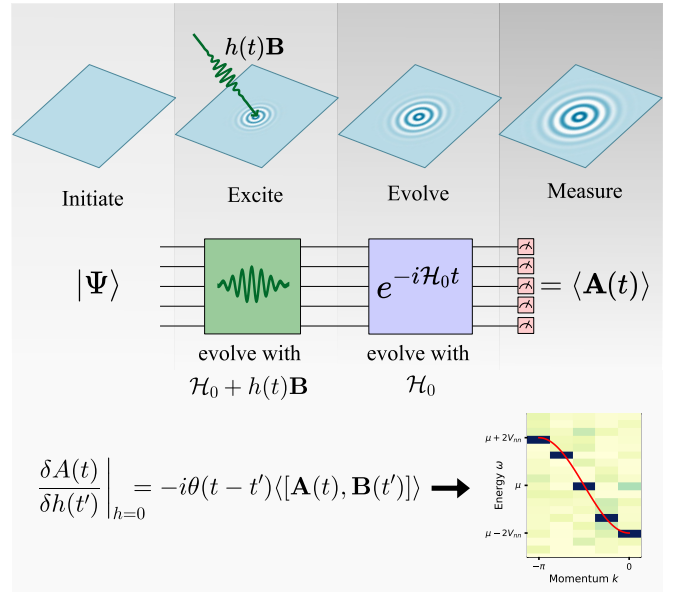


FIG. 1. **Linear response method.** We establish an equivalence between the experimental measurement of a response function and an ancilla-free quantum simulation under a time dependent Hamiltonian that includes the perturbative excitation $h(t)\mathbf{B}$. Following excitation, the system is evolved under \mathcal{H}_0 , and \mathbf{A} is measured. The functional derivative of $A(t) = \langle \mathbf{A}(t) \rangle$ with respect to $h(t')$ yields the retarded response function shown in the figure. The data shown is taken from Fig. 2.

tion function in the presence of decoherence and noise.

In this work, we outline a method for calculating correlation functions based on a *linear response* framework that is in direct correspondence to experiments, as schematically illustrated in Fig. 1. The quantum state is driven with an applied field with specific temporal and spatial structure, and the response of the system to that

* akemper@ncsu.edu

field is measured as a function of space and time. The proportionality between the field and the response then yield the desired correlation function(s).

The linear response framework has several advantages. First, a judicious choice of the applied field enables frequency- and momentum-selectivity in obtaining the desired correlation function(s); in particular, momentum-selectivity can significantly reduce circuit noise. Second, for systems that conserve total momentum, correlation functions in momentum space can be obtained with a single quantum circuit. And finally, the operators in the correlation function do not have to be unitary, and can even be non-Hermitian through block encoding[25].

We demonstrate the power of the linear response framework by applying it to the study of a model charge density wave system — the Su-Schrieffer-Heeger model[26]. We use the two fermionic methods with a momentum-selective field to obtain the electronic spectrum as would be measured by ARPES on IBM quantum hardware, and on a noisy simulator to compare the linear-response method to the Hadamard-test method. We next use the bosonic method and frequency selectivity to obtain the density-density response function of the same model system, as would be measured by momentum-resolved electron energy loss spectroscopy (M-EELS). These developments make significant inroads to being able to use near-term quantum computers in real-world applications.

This work also has impact on classical computing via a quantum inspired algorithm. The approach described below allows for one to compute response functions by simply running time evolution on a classical computer. This provides a different paradigm for computing response functions in exact diagonalization (and potentially other approaches, including matrix-product states) by mapping the problem onto time evolution with a time-dependent Hamiltonian. While our work here does not focus on this application, it should be clear that the approach developed here can be directly applied much more broadly.

RESULTS

Correlation functions are composed of expectation values of the form $\langle \mathbf{A}(r, t)\mathbf{B}(r', t') \pm \mathbf{B}(r', t')\mathbf{A}(r, t) \rangle$ — the amplitude of the operator \mathbf{A} at spacetime point (r, t) given that \mathbf{B} acted on the system at spacetime point (r', t') . The amplitudes are subtracted in the case of bosonic correlation functions, whereas they are added in the case of fermionic correlation functions. Both can be calculated via the *linear response* method that we present here. We will first describe the formalism for bosonic correlation functions and describe how to apply momentum and frequency selectivity. Then, we shall describe two different ways to apply the linear-response formalism to calculate fermionic correlation functions for Hamiltonians that conserve particle count parity (maintain even or

odd numbers of electrons).

Bosonic (commutator) correlation functions

The methodology employs the standard results from linear response in many-body physics (see e.g. Refs. 1, 2, and 27), as we develop below. We are interested in the expectation value of the operator $\mathbf{A}(t)$ measured in a prepared many-body state $|\psi_0\rangle$ and time-evolved in the Hamiltonian plus the applied (Hermitian) field; $h(t)\mathbf{B}$ that is, $\mathcal{H}(t) = \mathcal{H}_0 + h(t)\mathbf{B}$. Then, $A(t)$ is given by

$$A(t) = \langle \psi_0 | U(t)^\dagger \mathbf{A} U(t) | \psi_0 \rangle \quad (1a)$$

$$U(t) = \mathcal{T}_t e^{-i \int^t [\mathcal{H}_0 + \mathbf{B}h(\bar{t})] d\bar{t}}, \quad (1b)$$

where $U(t)$, in Eq. 1b, is the time ordered exponential for time evolution with respect to the time-dependent Hamiltonian plus field. Expanding $A(t)$ with respect to $h(t)$, we find

$$A(t) = \int dt' \chi^R(t, t') h(t') + \mathcal{O}(h^2). \quad (2)$$

Here, $\chi^R(t, t')$ is defined to be the functional derivative of $A(t)$ with respect to $h(t')$, which is given by

$$\left. \frac{\delta A(t)}{\delta h(t')} \right|_{h=0} = -i\theta(t - t') \langle \psi_0 | [\mathbf{A}(t), \mathbf{B}(t')] | \psi_0 \rangle. \quad (3)$$

In this result, we used the fact that $\mathbf{A}(t) := e^{it\mathcal{H}_0} \mathbf{A} e^{-it\mathcal{H}_0}$ in the limit of vanishing field. The θ -function arises because in Eq. 1b the integration region on the time ordered exponents is limited to \bar{t} values that are smaller than t . Since \mathcal{H}_0 is time independent, the response function $\chi^R(t, t')$ only depends on the time difference $t - t'$. Fourier transforming from time to frequency, and using the convolution theorem, yields

$$A(\omega) = \chi^R(\omega) h(\omega) + \mathcal{O}(h^2). \quad (4)$$

Thus, if the amplitude of the signal $h(t)$ is chosen to be small enough, the higher-order terms can be neglected and the response function can be calculated as a simple ratio.

Frequency selectivity: One might be interested in the response function centered in a specific frequency interval and want to improve the signal-to-noise ratio of the calculation. This is achieved by choosing the frequency support of $h(t)$ to be most concentrated within the desired frequency interval.

Momentum selectivity: By choosing \mathbf{A} and \mathbf{B} as operators with definite momentum, we can directly calculate the response function in the momentum basis. For example, for creation of a fermion with momentum k , we pick $\mathbf{B} = \sum_r e^{ikr} \tilde{X}_r + \text{H.C.} = \sum_r \cos(kr) \tilde{X}_r$, where \tilde{X}_r is $X_r Z_{r-1} \dots Z_0$. This can be directly implemented when

$|h(t)|\Delta t \ll 1$ with the expansion of the evolution for a single time step

$$e^{-ih(t)\mathbf{B}\Delta t} = \prod_r e^{-2ih(t)\Delta t \cos(kr)\tilde{X}_r} + \mathcal{O}(h^2). \quad (5)$$

We can use a similar form for \mathbf{A} as we use for \mathbf{B} , but since it is directly measured (rather than appearing in the time evolution), this can be achieved instead with multiple circuits. However, if \mathcal{H}_0 is translation invariant, only one circuit is sufficient to calculate the response function χ^R in momentum space because it satisfies

$$\chi_{k,k'}^R(t-t') = \delta_{k,k'} \chi_{k,k}^R(t-t'), \quad (6)$$

that is, it is diagonal in momentum.

Both momentum and frequency selectivity allow us to immediately focus the signal we obtain from the quantum computer into desired ranges of momentum or frequency. This frequency selectivity is not possible in the Hadamard test (as well as other approaches)[28, 29]. Moreover, implementing a momentum selective operator can only be achieved via costly circuit modifications such as embedding techniques. To avoid this, other approaches require each real space pair (r_1, r_2) to be measured separately with independent circuits; these are then Fourier transformed to obtain a momentum response function. On a fault-tolerant computer this might not have any difference, but on a noisy device, systematic errors can add from the different measurements, reducing the precision of the final result. In the following sections, we show that momentum selectivity in our approach significantly reduces noise in the measured signal.

Fermionic (anti-commutator) correlation functions

The most important fermionic correlation function is the retarded electronic Green's function given by

$$G^R(r_i, t; r_j, t') = -i\theta(t-t') \langle \psi_0 | \{c_i(t), c_j^\dagger(t')\} | \psi_0 \rangle, \quad (7)$$

where c_i and c_j^\dagger are the fermionic annihilation and creation operators at $r = r_i$ and r_j , respectively. Note that Eq. 7 is the correlation function with respect to a single many-body state $|\psi_0\rangle$. For the Green's function at $T = 0$ in standard many-body theory $|\psi_0\rangle$ is the ground state. At finite temperatures the expectation value has to be additionally averaged over a thermal distribution of states, which can be achieved via classical averaging of eigenstates[30–32] or by going over to a density matrix representation[25, 33–38]. The formalism below is applicable for any of these cases.

The functional derivative method does not directly carry over, because it requires adding a Grassman number valued field, which cannot be easily realized in a numerical simulation. This has thus far limited the potential of ancilla-free methods to bosonic correlation functions only[28, 29]. To overcome this, we introduce two

complementary approaches. The first uses an auxiliary operator \mathbf{P} which anti-commutes with \mathbf{B} , while the second uses simple post-selection.

Auxiliary Operator Method

We consider the fermionic version of Eq. (3), and denote this by $G(t, t')$:

$$G(t, t') = -i\theta(t-t') \langle \psi_0 | \{\mathbf{A}(t), \mathbf{B}(t')\} | \psi_0 \rangle. \quad (8)$$

In order to produce an anticommutator, we introduce an additional operator \mathbf{P} which satisfies the following properties

1. $\mathbf{P} |\psi_0\rangle = s |\psi_0\rangle$ with $s \neq 0$.
2. $\{\mathbf{B}(t), \mathbf{P}\} = 0$ for all times t .
3. $[\mathcal{H}_0, \mathbf{P}] = 0$, or \mathbf{P} has no time dependence.

With these properties, it is straightforward to show that

$$G(t, t') = \frac{i}{s} \theta(t-t') \langle \psi_0 | [\mathbf{A}(t)\mathbf{P}(t), \mathbf{B}(t')] | \psi_0 \rangle. \quad (9)$$

This is of the form of Eq. (3) with $\mathbf{A}(t)$ replaced by $\mathbf{A}(t)\mathbf{P}(t)$; therefore, the bosonic linear response method can be directly used.

Even though the assumptions on \mathbf{P} appear to be restrictive, when $G(t, t')$ is the retarded electronic Green's function, as in Eq. (7), the assumptions are satisfied by the parity operator for Hamiltonians that preserve particle parity; this covers a vast class of Hamiltonians of interest in quantum chemistry, condensed matter physics and quantum field theory. If the Hamiltonian of interest conserves the parity of the electron number, then the parity operator $\mathbf{P} = Z_1 Z_2 \dots Z_n$ satisfies second and third conditions, where we use the spin representation (obtained after Jordan-Wigner transformation) to represent the parity operator. The fermionic operators, c_i and c_i^\dagger , in their spin representation, have a Jordan-Wigner string attached; that is, they are composed of $i-1$ consecutive Z operators followed by a $X \pm iY$. In this case both c_i and c_i^\dagger anticommute with the parity operator $\mathbf{P} = Z_1 Z_2 \dots Z_n$, which satisfies the second condition. With this, $G(t, t')$ can be obtained by measuring Eq. (9) upon replacing \mathbf{A} with $X_i \mathbf{P}$ (and/or $Y_i \mathbf{P}$) and \mathbf{B} with X_j (and/or Y_j).

We can choose $h(t)$ and \mathbf{B} to have frequency and momentum selectivity in the same way as we did for bosonic correlation functions. Thus, we can directly calculate the fermionic Green's function in momentum space,

$$G^R(k, t; k', t') = -i\theta(t-t') \langle \psi_0 | \{c_k(t), c_{k'}^\dagger(t')\} | \psi_0 \rangle, \quad (10)$$

by selecting \mathbf{A} as a Fourier combination of $X_i \mathbf{P}$ (and/or $Y_i \mathbf{P}$) with momentum k , and \mathbf{B} as a Fourier combination

of X_j (and/or Y_j) with momentum k' , and forming the appropriate linear combination to select the desired c/c^\dagger terms. Similarly, by choosing an appropriate frequency support for $h(t)$, we can calculate G^R in a desired frequency range.

Post-selection for single-particle Green's functions

When the desired anti-commutator is the single-particle Green's function (Eq. 7) for a particle number conserving Hamiltonian, i.e. $|\psi_0\rangle$ is an N -particle wave function, a powerful alternate approach exists. A complete derivation is shown in App. C; we outline the salient

parts here. Let us specify our perturbing field as

$$\mathbf{B} = \sum_m \alpha_m \tilde{X}_m = \sum_m \alpha_m (c_m + c_m^\dagger), \quad (11)$$

where $\tilde{X}_m = Z_1 \dots Z_{m-1} X_m$. Position or momentum selectivity can be imposed by the choice of α_m . Starting from a wavefunction with N particles and evolving with $\mathcal{H}_0 + h(t)\mathbf{B}$, the system will be in a superposition of the $N-1$, N , and $N+1$ particle sectors to linear order in $h(t)$. For clarity, let us choose $h(t) = \eta\delta(t)$ where $\eta \ll 1$ and $\delta(t)$ is a Dirac delta pulse. This choice is not necessary, we can choose $h(t)$ more generally to achieve frequency selectivity. In order to measure the Green's function we apply a rotation about y (or x) to enable measurement of $c_1 \pm c_1^\dagger$ on the first qubit, which generates $N-2$ and $N+2$ particle states as well. Denoting $|\Phi_M^y\rangle$ (or $|\Phi_M^x\rangle$) as the M particle component of this final state, we observe that a simple post-selection that picks out one of the fixed particle number sectors yields

$$\langle \Phi_{N-1}^y | \Phi_{N-1}^y \rangle + \langle \Phi_{N+1}^y | \Phi_{N+1}^y \rangle = \frac{1}{2} + \eta \sum_m \alpha_m \text{Re} [G_{1m}^>(t) - G_{1m}^<(t)] = \frac{1}{2} + \eta \sum_m \alpha_m \text{Re} G_{1m}^R(t) \quad (12a)$$

$$\langle \Phi_N^y | c_1^\dagger c_1 | \Phi_N^y \rangle + \langle \Phi_{N+1}^y | \Phi_{N+1}^y \rangle = \frac{1}{2} + \eta \sum_m \alpha_m \text{Re} [G_{1m}^>(t) + G_{1m}^<(t)] \quad (12b)$$

$$\langle \Phi_{N-1}^x | \Phi_{N-1}^x \rangle + \langle \Phi_{N+1}^x | \Phi_{N+1}^x \rangle = \frac{1}{2} + \eta \sum_m \alpha_m \text{Im} [G_{1m}^>(t) - G_{1m}^<(t)] = \frac{1}{2} + \eta \sum_m \alpha_m \text{Im} G_{1m}^R(t) \quad (12c)$$

$$\langle \Phi_N^x | c_1^\dagger c_1 | \Phi_N^x \rangle + \langle \Phi_{N+1}^x | \Phi_{N+1}^x \rangle = \frac{1}{2} + \eta \sum_m \alpha_m \text{Im} [G_{1m}^>(t) + G_{1m}^<(t)] \quad (12d)$$

where the fermionic Green's functions are[1],

$$\begin{aligned} G_{ij}^<(t) &= i \langle \psi_0 | c_j^\dagger(0) c_i(t) | \psi_0 \rangle \\ G_{ij}^>(t) &= -i \langle \psi_0 | c_i(t) c_j^\dagger(0) | \psi_0 \rangle \\ G_{ij}^R(t) &= -i\theta(t) \langle \psi_0 | \{c_i(t), c_j^\dagger(0)\} | \psi_0 \rangle. \end{aligned} \quad (13)$$

The quantities in Eq. 12 can be obtained simply by considering the probabilities of states with specific particle number. While this is limited to particle-conserving Hamiltonians, this is a relatively mild restriction as all fermionic Hamiltonians that do not have superconducting terms satisfy this restriction.

Algorithmic and analysis details

Here, we outline the details of the implementation and the signal analysis. One noteworthy aspect is the use of a damping function $g(t)$. In many-body physics, an $\exp(-\gamma t)$ convergence factor is often used to regularize otherwise divergent Fourier integrals, where $\gamma > 0$

[1, 2, 27]. Moreover, in realistic materials, sharp peaks in the spectrum are broadened due to the natural interactions that occur. The damping function $g(t)$ is an effective way to incorporate these effects. Practically speaking, enforcing the signal to decay has a benefit from the quantum circuit perspective: namely, it limits the maximum simulation time necessary, which in turn limits the circuit depth.

Here, we consider it an adjustable function that softens the Fourier spectra by ensuring the signal has compact support in the time domain. Applying an exponential decay factor to the signal is equivalent to a Lorentzian broadening in the frequency domain, and sets the effective resolution of this approach. Similarly, the natural noise inherent in quantum hardware where the circuit depth grows with increasing time may perform a similar function.

The procedure to obtain the correlation function given a state of interest $|\psi_0\rangle$ is as follows

1. Evolve $|\psi_0\rangle$ with the perturbed Hamiltonian $\mathcal{H}(t) = \mathcal{H}_0 + h(t)\mathbf{B}$ during the time where $h(t)$ is

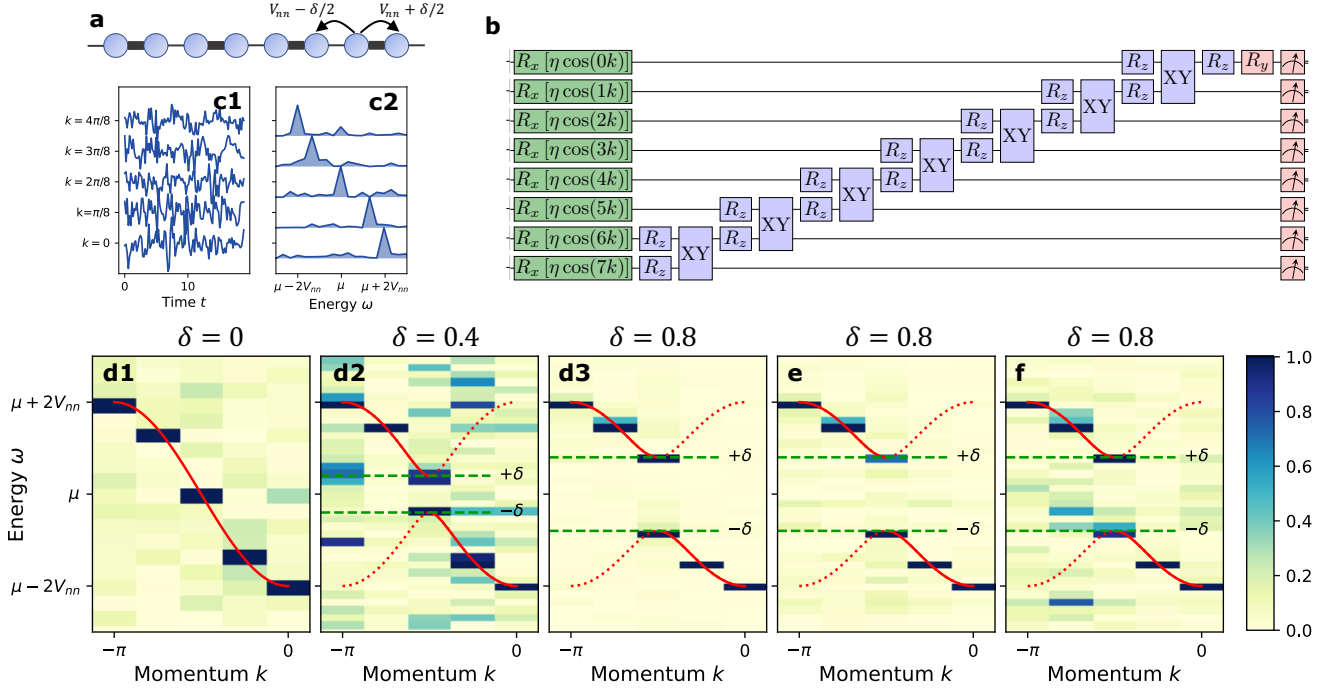


FIG. 2. **Electronic Green's function for the Su-Schrieffer-Heeger (SSH) model.** **a.** Lattice and hopping structure of the SSH model. **b.** Compressed linear response method quantum circuit run on *ibm.auckland*. XY indicates a rotation about XX followed by YY[39, 40]. **c1.** Fermionic correlation function $\mathcal{L}_k(t) = 2 \text{Re } G_k(t)$ for $\delta = 0$ using the commutator method. Data for other values of δ are available in the SI. **c2.** Normalized power spectrum $|\mathcal{L}_k(\omega)|^2$. **d.** Normalized false-color plots of $|\mathcal{L}_k(\omega)|^2$ for $\delta = \{0, 0.4, 0.8\}$. Green dashed lines indicate the expected bounds of the gap, and the red lines the analytically obtained spectrum. **e, f.** Normalized false-color plot of post-selected $\langle \Phi_0^y | \Phi_0^y \rangle$ and $\langle \Phi_1^y | \Phi_1^y \rangle$, respectively (see text for definition). The projected norms contain the same spectral information as $\mathcal{L}_k(\omega)$.

finite. $h(t)$ should be a small field in order to ensure the simulation is in the linear response regime. This can be tested by repeating the simulation with larger/smaller $h(t)$ and checking that the response scales similarly.

2. Continue to evolve with the unperturbed Hamiltonian \mathcal{H} . The maximum length of time needed is set by the desired minimum energy resolution.
3. At each time of interest t , measure $A(t) = \langle \mathbf{A}(t) \rangle$.
4. Apply a semi-phenomenological damping function such as $g(t) = \exp(-t/\tau)$ to obtain $\tilde{A}(t) = g(t)A(t)$. This sets an effective energy resolution τ^{-1} in the susceptibility. This approach was recently shown to additionally help by limiting the circuit depth required[41].
5. Fourier transform $\tilde{A}(t)$ to $A(\omega)$ and divide by $h(\omega)$ to obtain $\chi(\omega)$, thus performing the (numerical) functional differentiation.

Green's function of the SSH model.

We demonstrate the linear response approach by calculating the fermionic Green's function as would be measured by ARPES (angle-resolved photoemission spectroscopy). We study a minimal model for a charge density wave known as the Su-Schrieffer-Heeger (SSH) model — an N-site 1D free fermionic chain with nearest-neighbor bond-dependent hoppings (see Fig. 2a) — in the limit where the lattice distortion is static,

$$\mathcal{H}_0 = - \sum_{\langle i,j \rangle} \left[V_{nn} + (-1)^i \delta/2 \right] c_i^\dagger c_j - \mu \sum_i c_i^\dagger c_i. \quad (14)$$

For finite δ this model exhibits a charge density wave, with a gap proportional to δ . Since this is a free fermionic system, the spectrum is easily obtained by starting from the vacuum state, so we set $\mu = 5$ to suppress the initial total electron number.

We use a momentum-selective instantaneous (and thus broadband) driving field coupled to the particle creation and annihilation operators that act on all the sites i ,

$$\mathbf{B} = \sum_i 2 \cos(kr_i) \left[c_i + c_i^\dagger \right], \quad (15)$$

with a pulse $h(t) = \eta\delta(t)$, where we used $\eta dt = 0.04$. We measure $X_0 = c_0 + c_0^\dagger$ which is local in position, and includes all momentum modes. Because \mathcal{H}_0 for the SSH model conserves momentum, by measuring X_0 we obtain $\mathcal{L}_k(t) = 2 \text{Re } G_k(t)$ which has the full information of the single particle spectral function; in the frequency basis, this is (see Appendix D for details)

$$\mathcal{L}_k(\omega) = G_k(\omega) + G_k(-\omega)^*. \quad (16)$$

Even though our method is capable of measuring $G_k(\omega)$, isolating it from $G_k(-\omega)^*$ requires running the same circuit and measuring Y_0 as well. Since $\mu = 5$, for this model the single particle energies are manifestly positive, and the interference between $G_k(\omega)$ and $G_k(-\omega)$ is negligible. Thus, $|\mathcal{L}_k(\omega)|^2$ tracks the quasi-particle peaks in $\text{Im } G_k(\omega)$, and measuring $\mathcal{L}_k(\omega)$ is sufficient to obtain the single-particle spectrum.

On the quantum computer, the driving field is implemented in a single Trotter step; a set of single-qubit x -rotations with an amplitude $2h_0 \cos(kr_j)$ on the j -th qubit. The subsequent evolution uses compressed free fermionic evolution [39, 40]. To minimize the weight of the measured Pauli string (and thus reduce measurement noise) we perform the measurement on the 1st qubit. To further mitigate error, we use Pauli twirling and dynamic decoupling[42]. Additional details of the quantum computation may be found in the supplementary material.

We performed the calculation on *ibm_auckland* for an $N = 8$ -site chain, which has allowed momentum values $k = \frac{2\pi}{N}j, j \in \{0 \dots 7\}$. Since the driving field \mathbf{B} is symmetric in k , both k and $-k$ are obtained at the same time. We used a compressed form of the quantum circuit shown in panel **b** (check Appendix D 2 for details). Fig. 2 panel **c1** shows the raw data for $\mathcal{L}_k(t)$ with $\delta = 0$ at each unique k ; the data was obtained from *ibm_auckland* via the parity operator method. The power spectrum is shown in panels **c2** and **d1**. While the data from the quantum computer appears quite noisy, in the frequency regime of interest there is only a single peak present in the Fourier transform, illustrating the remarkable strength of a momentum-selective probe, which picks out the single energy at each momentum, together with Fourier filtering. Upon increasing δ (panels **d2,d3**), a gap opens up in the spectrum (time traces and Fourier amplitudes are available in Appendix A). The spectrum for $\delta = 0.4$ is noisier than the other two, which we attribute to machine noise from those particular measurements. In panels **e,f**, we plot the norms of 0- and 1- particle components of the state right before the measurement, i.e. $\langle \Phi_0^y | \Phi_0^y \rangle$ and $\langle \Phi_1^y | \Phi_1^y \rangle$, where $|\Phi_M^y\rangle$ is defined above Eq. 12. Both of these partial norms are equivalent to $\mathcal{L}_k(t)$ (See Appendix C 2 for details). Both methods faithfully reproduce the power spectrum, with slightly higher levels of noise for post-selection on $N = 1$.

In order to further underscore the power of the momentum-selective linear response approach, we compare its effectiveness to a position-selective linear response and Hadamard test methods in Fig. 3 on a noisy

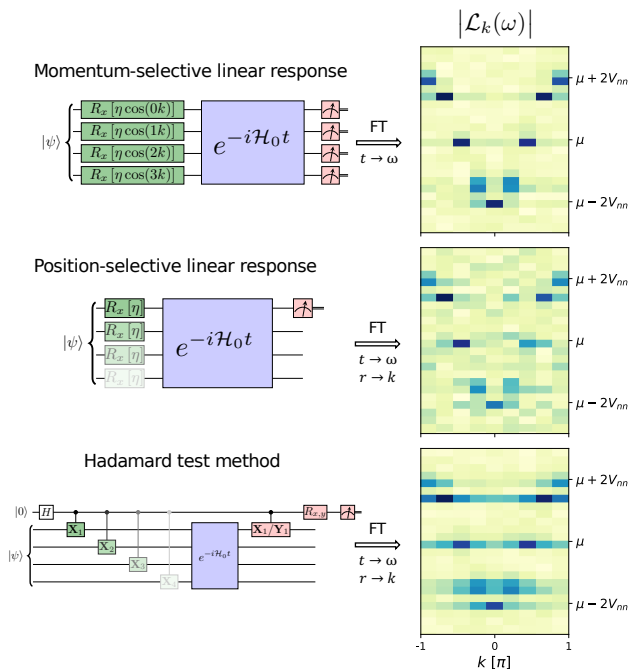


FIG. 3. **Comparison of the momentum selective linear response, position selective linear response, and Hadamard test methods.** The circuit diagrams schematically represent the 3 approaches, which were run on a noisy simulators with one/two qubit noise of 1% and 10%, respectively. While the momentum selective linear response method directly yields $\mathcal{L}_k(t)$, an additional spatial Fourier transformation is needed for the other two methods.

simulator (see Appendix B for details of the simulation and detailed analysis). Compared to the momentum-selective linear response method, the position-selective one is noisier, but without particular structure. The Hadamard test, on the other hand, exhibits streaks that arise from leakage of signal from one momentum to the others. There are two key reasons for the differences seen in the figure. First, both position-selective and Hadamard test methods involve excitations at each position (X_i in the figure). These must be combined in the post-processing with a Fourier transform. But, because a Fourier transform relies on constructive/destructive interference between signals, and we are performing this on noisy data, the interference is not perfect, which leads to leakage between momentum channels. Second, the Hadamard test method introduces more of the same problem because each X_i is a separate circuit — in addition to needing more circuits to be run and an additional ancilla. This further exacerbates the issue with the Fourier analysis. The momentum-selectivity avoids these issues by making a unique excitation and thus producing a response function with a single large contribution.

Polarizability of the SSH model

We next consider the polarizability $\chi(q, \omega)$ of the 1D chain. The polarizability is the response of the electronic system to an applied potential. It plays a critical role in the screening of interactions between electrons in solids and molecules, and in their electromagnetic properties. Experimentally, the polarizability can be studied by light absorption or scattering, or by momentum-resolved electron energy loss spectroscopy (M-EELS). The polarizability is defined by

$$\chi(r, t) = -i \langle \psi_0 | \delta n(r, t) \delta n(r=0, t=0) | \psi_0 \rangle, \quad (17)$$

i.e. it is a charge-charge correlation function. Here δn is the change in the charge from the equilibrium density. The observable \mathbf{A} is the charge, and the applied field \mathbf{B} (which is conjugate to the charge) is a potential. The excitations are changes in the density, which are composed of pairs of fermionic operators, and thus this is a bosonic correlation function.

For this demonstration, \mathbf{B} acts on a single site, and we classically simulate a partially filled 24-site chain ($\mu = 0.9$). As discussed above, one of the advantages of the linear response framework is that all 24 correlation functions are obtained with a single calculation. Fig. 4a shows $\text{Im } \chi(q, \omega)$, which is the double Fourier transform of $\chi(r, t)$ obtained from driving a single site with a sharp $h(t)$. $\text{Im } \chi(q, \omega)$ has all the textbook features of the response of a 1D charged system; there is no response at all at $q = 0$ due to charge conservation, there is a narrow dispersive feature at low q, ω that broadens with increasing q , and a low-energy turnover with a minimum at $2k_F$.

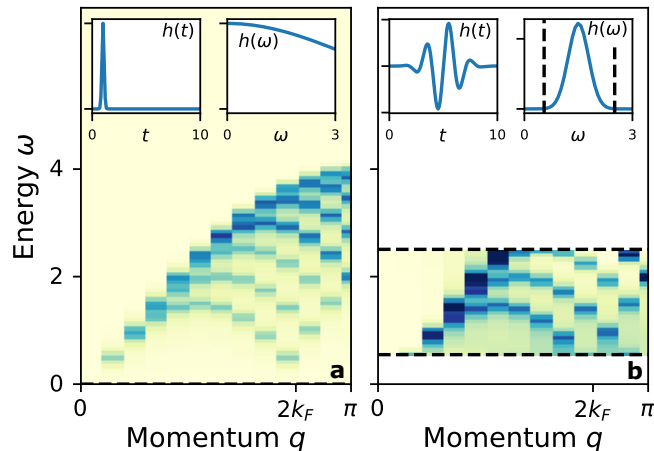


FIG. 4. **Polarizability for the 1D chain.** Both panels show $\text{Im } \chi(q, \omega)$ in false color. The insets show the driving field $h(t)$ and its Fourier transform. **a.** $\chi(q, \omega)$ obtained from the response due to a sharp excitation with height 0.1. **b.** $\chi(q, \omega)$ obtained from the response of a frequency selective field. The dashed lines indicate the range where $|h(\omega)|^2 < 10^{-3}$. Here, we used $h(t)$ as sinusoid with a Gaussian profile of width $\sigma = 0.625$, height 0.05, and centered at $\omega = 1.5$.

Since $h(\omega)$ has support across the entire spectrum of $\chi(q, \omega)$ (shown in the inset), the entire spectrum can be obtained from this measurement. This is in contrast to panel **b**, where we drive with a short-duration sinusoid centered at $\omega = 1.5$. This excitation is *frequency-selective*; that is, it only excites the system at frequencies where $h(\omega)$ has finite support. This range of frequencies is indicated by dashed lines in the figure. With our particular choice of $h(t)$ we are able to observe some of the middle range of excitations, but are insensitive to the lower frequencies and the top of the spectrum. Note that there is no restriction on the Fourier transform of $\chi(r, t)$ per se; rather, the need to divide by $h(\omega)$ (see Eq. 3) limits the applicable window to the ranges where $h(\omega)$ is finite.

DISCUSSION

The linear-response based formalism is a shift in perspective on quantum simulation; the measurement process is truly a part of the simulation as an experimental driving field. This is in contrast to Hadamard-test and other competing approaches, where the simulation is limited to the system, and the desired observables are extracted either outside of the system qubits and/or from a large excitation. This shift in perspective and methodology enables a much broader set of observables to be envisioned and easily calculated, and enables a direct connection to experiment. Moreover, it relies almost entirely on time evolution, a task for which quantum computers are naturally suited.

This shift in perspective and the resulting implementation leads to several clear advantages. First, mirroring experimental procedure, we can straightforwardly achieve momentum- and frequency selectivity by focusing the perturbation $h(t)\mathbf{B}$ on a certain momentum or frequency range, without difficulty or additional implementation cost. This is enabled on the quantum circuit level by an implementation advantage of the linear response: \mathbf{B} can be chosen to be non-unitary because we apply $e^{-ih(t)\mathbf{B}\Delta t}$, as opposed to the Hadamard test which applies \mathbf{B} on the state. The resulting momentum selectivity produces less noise in the response functions (c.f. Fig. 3) because the calculation is done via one circuit rather than certain linear combinations of results obtained from structurally different circuits with different noise. This advantage is particularly underscored for translationally-invariant systems where momentum is a good quantum number; enforcing the momentum selectivity on \mathbf{B} and running only one circuit per momentum k is sufficient to measure the response in momentum basis because $\chi_{k, k'}^R$ is diagonal. The resulting signal will thus have a fixed number of frequency peaks for given k value (c.f. Figs. 2 and 3), simplifying the signal processing.

Fermionic response functions (anti-correlation functions) can be obtained with the same experimentally centered, linear response perspective; this is unlike other

ancilla-free methods[28, 29] which are limited to bosonic response functions. The post-selection method is intuitive, as the particle number sectors are clearly delineated. On the other hand, the auxiliary operator method is an unusual perspective; it is sufficient to measure almost the same operator as for the bosonic correlation function. The electron Green’s function, for example, is obtained simply by keeping track of the parity as well as the occupation number measurement. In either case, this is an important advance since electron Green’s functions play a key role in physics; as an important measurement per se[43], and as an ingredient in embedding theories such as dynamical mean field theory [3–8].

While here we have explicitly demonstrated the linear response approach in the context of a charge density wave, it is a general method to obtain response functions, and is not limited to electronic Hamiltonians. It can be applied to spin or bosonic models, or other models from fields where quantum simulation plays a role, including chemistry and high energy physics. Different choices of \mathbf{A} and \mathbf{B} extend the method to a wide variety of observables. For example, the conductivity is a current-current correlation function, for which $h(t)$ is an applied electric field. A zz -spin susceptibility can be obtained with $h(t)$ as a z -axis magnetic field, and the operators $\mathbf{A} = \mathbf{B} = S_z$. Moving forward, the functional derivative formalism can be extended to higher order derivatives that involve multiple driving fields. One notable application is resonant inelastic X-ray scattering (RIXS), which is a four-point correlation function[44], which is very challenging to calculate via diagrammatics. In addition, and aside from direct experimental probes, pairing vertices in superconductors and other ordered phenomena also fall into this class of observables. We reserve these discussions for future work.

This approach is a quantum-inspired paradigm, which can also be applied in conventional computation. Rather than having to measure all of the different matrix elements needed for the Lehmann formula, this approach requires simulating time-evolution and then measuring the expectation value of a single operator. As such, it

is likely to be much more efficient than currently used methods.

MATERIALS AND METHODS

The data shown in Fig. 2 was calculated on *ibm_auckland*. For each k and δ we collected 3 data sets with 8,000 shots each, yielding 24,000 shots total per curve. While no measurement error mitigation was used, we incorporated dynamical decoupling and Pauli twirling as implemented in the *qiskit_research* package. The raw data is shown in the supplementary material in Fig. S1. The calibration data is shown in tables S1 and S2.

ACKNOWLEDGMENTS

We acknowledge helpful discussions with Erik Gustafson and Vito Scarola. We acknowledge the use of IBM Q via the IBM Q Hub at North Carolina (NC) State for this paper. The views expressed are those of the authors and do not reflect the official policy or position of the IBM Q Hub at NC State, IBM or the IBM Q team. We acknowledge the use of the QISKIT software package [42] for performing the quantum simulations. **Funding:** This work was supported by the Department of Energy, Office of Basic Energy Sciences, Division of Materials Sciences and Engineering under grant no. DE-SC0023231. J.K.F. was also supported by the McDevitt bequest at Georgetown. Author contributions: A.F.K. and J.K.F. conceptualized the project. A.F.K. developed the methodology, performed the quantum computer experiments, and ran the polarizability calculations. E.K. contributed to the mathematical development for fermionic response functions and designed the quantum circuits. H.A.L. ran the noisy quantum simulator calculations. All authors discussed the results and contributed to the development of the manuscript. **Competing interests:** The authors declare that they have no competing interests. **Data and materials availability:** All data needed to evaluate the conclusions in the paper are present in the paper and/or the Supplementary Materials.

-
- [1] G. D. Mahan, *Many Particle Physics* (Springer, New York, NY10013, USA, 2010).
 - [2] G. Stefanucci and R. van Leeuwen, *Nonequilibrium Many-Body Theory of Quantum Systems: A Modern Introduction*, 1st ed. (Cambridge University Press, 2013).
 - [3] A. Georges, G. Kotliar, W. Krauth, and M. J. Rozenberg, *Reviews of Modern Physics* **68**, 13 (1996).
 - [4] D. Zgid and G. K.-L. Chan, *J. Chem. Phys.* **134** (2011).
 - [5] I. Rungger, N. Fitzpatrick, H. Chen, C. H. Alderete, H. Apel, A. Cowtan, A. Patterson, D. M. Ramo, Y. Zhu, N. H. Nguyen, E. Grant, S. Chretien, L. Wossnig, N. M. Linke, and R. Duncan, “Dynamical mean field theory algorithm and experiment on quantum computers,” (2020), [arXiv:1910.04735 \[quant-ph\]](https://arxiv.org/abs/1910.04735).
 - [6] T. Keen, T. Maier, S. Johnston, and P. Lougovski, *Quantum Science and Technology* **5**, 035001 (2020).
 - [7] T. Steckmann, T. Keen, A. F. Kemper, E. F. Dumitrescu, and Y. Wang, arXiv preprint arXiv:2112.05688 (2021).
 - [8] F. Jamet, A. Agarwal, and I. Rungger, arXiv preprint arXiv:2205.00094 (2022).
 - [9] A. Chiesa, F. Tacchino, M. Grossi, P. Santini, I. Tavernelli, D. Gerace, and S. Carretta, *Nature Physics* **15**, 455 (2019).
 - [10] A. Roggero and J. Carlson, *Phys. Rev. C* **100**, 034610 (2019).

- [11] A. Francis, J. K. Freericks, and A. F. Kemper, *Phys. Rev. B* **101**, 014411 (2020).
- [12] T. Kosugi and Y. I. Matsushita, *Physical Review A* **101**, 1 (2020).
- [13] T. Kosugi and Y.-i. Matsushita, *Phys. Rev. Research* **2**, 033043 (2020).
- [14] S. Endo, I. Kurata, and Y. O. Nakagawa, *Phys. Rev. Research* **2**, 033281 (2020).
- [15] F. Libbi, J. Rizzo, F. Tacchino, N. Marzari, and I. Tavernelli, arXiv preprint arXiv:2203.12372 (2022).
- [16] H. Chen, M. Nusspickel, J. Tilly, G. H. Booth, *et al.*, *Physical Review A* **104**, 032405 (2021).
- [17] G. Gyawali and M. J. Lawler, arXiv preprint arXiv:2109.12126 (2021).
- [18] C. K. Lee, S.-X. Zhang, C.-Y. Hsieh, S. Zhang, and L. Shi, arXiv preprint arXiv:2206.05571 (2022).
- [19] P. W. K. Jensen, P. D. Johnson, and A. A. Kunitsa, arXiv preprint arXiv:2206.09881 (2022).
- [20] K. Huang, X. Cai, H. Li, Z.-Y. Ge, R. Hou, H. Li, T. Liu, Y. Shi, C. Chen, D. Zheng, *et al.*, *The Journal of Physical Chemistry Letters* **13**, 9114 (2022).
- [21] A. Ciavarella, *Phys. Rev. D* **102**, 094505 (2020).
- [22] A. Roggero, *Phys. Rev. A* **102**, 022409 (2020).
- [23] T. Keen, E. Dumitrescu, and Y. Wang, arXiv preprint arXiv:2112.05731 (2021).
- [24] Y. Tong, D. An, N. Wiebe, and L. Lin, *Phys. Rev. A* **104**, 032422 (2021).
- [25] A. Gilyén, Y. Su, G. H. Low, and N. Wiebe, in *Proceedings of the 51st Annual ACM SIGACT Symposium on Theory of Computing* (2019) pp. 193–204.
- [26] W. P. Su, J. R. Schrieffer, and A. J. Heeger, *Phys. Rev. Lett.* **42**, 1698 (1979).
- [27] H. Bruus and K. Flensberg, *Many-body quantum theory in condensed matter physics: an introduction* (OUP Oxford, 2004).
- [28] E. Gustafson, B. Holzman, J. Kowalkowski, H. Lamm, A. C. Y. Li, G. Perdue, S. Boixo, S. Isakov, O. Martin, R. Thomson, C. V. Heidweiller, J. Beall, M. Ganahl, G. Vidal, and E. Peters, (2021), [10.48550/ARXIV.2110.07482](https://arxiv.org/abs/10.48550/ARXIV.2110.07482).
- [29] P. Uhrich, S. Castrignano, H. Uys, and M. Kastner, *Phys. Rev. A* **96**, 022127 (2017).
- [30] S. R. White, *Physical review letters* **102**, 190601 (2009).
- [31] G. Verdon, J. Marks, S. Nanda, S. Leichenauer, and J. Hidary, arXiv preprint arXiv:1910.02071 (2019).
- [32] J. Cohn, F. Yang, K. Najafi, B. Jones, and J. K. Freericks, *Phys. Rev. A* **102**, 022622 (2020).
- [33] D. Poulin and P. Wocjan, *Physical review letters* **103**, 220502 (2009).
- [34] M. Motta, C. Sun, A. T. Tan, M. J. O’Rourke, E. Ye, A. J. Minnich, F. G. Brandão, and G. K.-L. Chan, *Nature Physics* **16**, 205 (2020).
- [35] M. Metcalf, J. E. Moussa, W. A. de Jong, and M. Sarovar, *Physical Review Research* **2**, 023214 (2020).
- [36] S. Polla, Y. Herasymenko, and T. E. O’Brien, arXiv preprint arXiv:1909.10538 (2019).
- [37] D.-B. Zhang, G.-Q. Zhang, Z.-Y. Xue, S.-L. Zhu, and Z. Wang, arXiv preprint arXiv:2006.00471 (2020).
- [38] M. Metcalf, E. Stone, K. Klymko, A. F. Kemper, M. Sarovar, and W. A. de Jong, arXiv preprint arXiv:2103.03207 (2021).
- [39] E. Kökcü, D. Camps, L. Bassman, J. K. Freericks, W. A. de Jong, R. Van Beeumen, and A. F. Kemper, *Physical Review A* **105**, 032420 (2022).
- [40] D. Camps, E. Kökcü, L. Bassman, W. A. de Jong, A. F. Kemper, and R. V. Beeumen, *SIAM Journal on Matrix Analysis and Applications* **43**, 1084 (2022).
- [41] W.-R. Lee, R. Scott, and V. Scarola, arXiv preprint arXiv:2212.14039 (2022).
- [42] M. S. ANIS, Abby-Mitchell, H. Abraham, AduOffei, R. Agarwal, G. Agliardi, M. Aharoni, I. Y. Akhalwaya, G. Aleksandrowicz, T. Alexander, M. Amy, S. Anagolum, Anthony-Gandon, E. Arbel, A. Asfaw, A. Athalye, A. Avkhadiev, C. Azaustre, P. Bhole, A. Banerjee, S. Banerjee, W. Bang, A. Bansal, P. Barkoutsos, A. Barnawal, G. Barron, G. S. Barron, L. Bello, Y. Ben-Haim, M. C. Bennett, D. Bevenius, D. Bhatnagar, A. Bhobe, P. Bianchini, L. S. Bishop, C. Blank, S. Bolos, S. Bopardikar, S. Bosch, S. Brandhofer, Brandon, S. Bravyi, N. Bronn, Bryce-Fuller, D. Bucher, A. Burov, F. Cabrera, P. Calpin, L. Capelluto, J. Carballo, G. Carrascal, A. Carriker, I. Carvalho, A. Chen, C.-F. Chen, E. Chen, J. C. Chen, R. Chen, F. Chevallier, K. Chinda, R. Cholarajan, J. M. Chow, S. Churchill, CisterMoke, C. Claus, C. Clauss, C. Clothier, R. Cocking, R. Cocuzzo, J. Connor, F. Correa, Z. Crockett, A. J. Cross, A. W. Cross, S. Cross, J. Cruz-Benito, C. Culver, A. D. Córcoles-Gonzales, N. D. S. Dague, T. E. Dandachi, A. N. Dangwal, J. Daniel, M. Daniels, M. Dartiailh, A. R. Davila, F. Debouni, A. Dekusar, A. Deshmukh, M. Deshpande, D. Ding, J. Doi, E. M. Dow, P. Downing, E. Drechsler, E. Dumitrescu, K. Dumon, I. Duran, K. EL-Safty, E. Eastman, G. Eberle, A. Ebrahimi, P. Eendebak, D. Egger, ElePT, Emilio, A. Espiricueta, M. Everitt, D. Facoetti, Farida, P. M. Fernández, S. Ferracin, D. Ferrari, A. H. Ferrera, R. Fouilland, A. Frisch, A. Fuhrer, B. Fuller, M. GEORGE, J. Gacon, B. G. Gago, C. Gambella, J. M. Gambetta, A. Gammanpila, L. Garcia, T. Garg, S. Garion, J. R. Garrison, J. Garrison, T. Gates, H. Georgiev, L. Gil, A. Gilliam, A. Giridharan, J. Gomez-Mosquera, Gonzalo, S. de la Puente González, J. Gorzinski, I. Gould, D. Greenberg, D. Grinko, W. Guan, D. Guijo, J. A. Gunnels, H. Gupta, N. Gupta, J. M. Günther, M. Haglund, I. Haide, I. Hamamura, O. C. Hamido, F. Harkins, K. Hartman, A. Hasan, V. Havlicek, J. Hellmers, L. Herok, S. Hillmich, H. Horii, C. Howington, S. Hu, W. Hu, J. Huang, R. Huisman, H. Imai, T. Imamichi, K. Ishizaki, Ishwor, R. Iten, T. Itoko, A. Ivrii, A. Javadi, A. Javadi-Abhari, W. Javed, Q. Jianhua, M. Jivrajani, K. Johns, S. Johnstun, Jonathan-Shoemaker, JosDenmark, JoshDumo, J. Judge, T. Kachmann, A. Kale, N. Kanazawa, J. Kane, Kang-Bae, A. Kapila, A. Karazeev, P. Kassebaum, T. Kehrer, J. Kelso, S. Kelso, V. Khanderao, S. King, Y. Kobayashi, Kovi11Day, A. Kovyrrshin, R. Krishnakumar, V. Krishnan, K. Krsulich, P. Kumkar, G. Kus, R. LaRose, E. Lacal, R. Lambert, H. Landa, J. Lapeyre, J. Latone, S. Lawrence, C. Lee, G. Li, J. Lishman, D. Liu, P. Liu, Lolcroc, A. K. M, L. Madden, Y. Maeng, S. Maheshkar, K. Majmudar, A. Malyshev, M. E. Mandouh, J. Manela, Manjula, J. Marecek, M. Marques, K. Marwaha, D. Maslov, P. Maszota, D. Mathews, A. Matsuo, F. Mazhandu, D. McClure, M. McElaney, C. McGarry, D. McKay, D. McPherson, S. Meesala, D. Meirom, C. Mendell, T. Metcalfe, M. Mevissen, A. Meyer, A. Mezzacapo, R. Midha, D. Miller, Z. Mineev, A. Mitchell, N. Moll, A. Montanez, G. Monteiro, M. D. Mooring, R. Morales, N. Moran, D. Morcuende,

S. Mostafa, M. Motta, R. Moyard, P. Murali, D. Murata, J. Müggenburg, T. NEMOZ, D. Nadlinger, K. Nakanishi, G. Nannicini, P. Nation, E. Navarro, Y. Naveh, S. W. Neagle, P. Neuweiler, A. Ngoueya, T. Nguyen, J. Nicander, Nick-Singstock, P. Niroula, H. Norlen, NuoWenLei, L. J. O’Riordan, O. Ogunbayo, P. Ollitrault, T. Onodera, R. Otaolea, S. Oud, D. Padilha, H. Paik, S. Pal, Y. Pang, A. Panigrahi, V. R. Pascuzzi, S. Perriello, E. Peterson, A. Phan, K. Pilch, F. Piro, M. Pistoia, C. Piveteau, J. Plewa, P. Pocreau, A. Pozas-Kerstjens, R. Pracht, M. Prokop, V. Prutyaynov, S. Puri, D. Puzzuoli, J. Pérez, Quant02, Quintiii, R. I. Rahman, A. Raja, R. Rajeev, I. Rajput, N. Ramagiri, A. Rao, R. Raymond, O. Reardon-Smith, R. M.-C. Redondo, M. Reuter, J. Rice, M. Riedemann, Rietesh, D. Risinger, M. L. Rocca, D. M. Rodríguez, RohithKarur, B. Rosand, M. Rossmannek, M. Ryu, T. SAPV, N. R. C. Sa, A. Saha, A. Ash-Saki, S. Sanand, M. Sandberg, H. Sandesara, R. Sapra, H. Sargsyan, A. Sarkar, N. Sathaye, B. Schmitt, C. Schnabel, Z. Schoenfeld, T. L. Scholten, E. Schoute, M. Schulterbrandt, J. Schwarm, J. Seaward, Sergi, I. F. Sertage, K. Setia, F. Shah, N. Shammah, R. Sharma, Y. Shi, J. Shoemaker, A. Silva, A. Simonetto, D. Singh, D. Singh, P. Singh, P. Singkanipa, Y. Siraichi, Siri, J. Sistos, I. Sitdikov, S. Sivarajah, Slavikmew, M. B. Sletfjerd- ing, J. A. Smolin, M. Soeken, I. O. Sokolov, I. Sokolov, V. P. Soloviev, SooluThomas, Starfish, D. Steenken, M. Stypulkoski, A. Suau, S. Sun, K. J. Sung, M. Suwama, O. Słowik, H. Takahashi, T. Takawale, I. Tavernelli, C. Taylor, P. Taylour, S. Thomas, K. Tian, M. Tillet, M. Tod, M. Tomasik, C. Tornow, E. de la Torre, J. L. S. Tournal, K. Trabing, M. Treinish, D. Trenev, TrishaPe, F. Truger, G. Tsilimigkounakis, D. Tulsi, W. Turner, Y. Vakinin, C. R. Valcarce, F. Varchon, A. Vartak, A. C. Vazquez, P. Vijaywargiya, V. Villar, B. Vishnu, D. Vogt- Lee, C. Vuillot, J. Weaver, J. Weidenfeller, R. Wiczorek, J. A. Wildstrom, J. Wilson, E. Winston, WinterSoldier, J. J. Woehr, S. Woerner, R. Woo, C. J. Wood, R. Wood, S. Wood, J. Wootton, M. Wright, L. Xing, J. YU, B. Yang, U. Yang, J. Yao, D. Yeralin, R. Yonekura, D. Yonge-Mallo, R. Yoshida, R. Young, J. Yu, L. Yu, C. Zachow, L. Zdanski, H. Zhang, I. Zidarur, B. Zimmermann, C. Zoufal, aeddins ibm, alexzhang13, b63, bartek bartlomiej, bcamorrison, brandhsn, charmer- Dark, deeplokhande, dekel.meirom, dime10, dlasecki, ehchen, fanizzamarco, fs1132429, gadial, galeinston, georgezhou20, georgios ts, gruu, hhorii, hykavitha, itoko, jeppevinkel, jessica angel7, jezerjojo14, jliu45, jscott2, klinvill, krutik2966, ma5x, michelle4654, msuwama, nico lgrs, nrhawkins, ntgiwsvp, ordmoj, sagar pahwa, pri- tamsinha2304, ryancocuzzo, saktar unr, saswati qiskit, septembr, sethmerkel, sg495, shaashwat, smturro2, sternparky, strickroman, tigerjack, tsura crisaldo, up- sideon, vadebayo49, welien, willhbang, wmurphy collab- star, yang.luh, and M. Čepulkovskis, “[Qiskit: An open- source framework for quantum computing](#),” (2021).

[43] A. Damascelli, Z. Hussain, and Z.-X. Shen, *Reviews of modern physics* **75**, 473 (2003).

[44] L. J. Ament, M. Van Veenendaal, T. P. Devereaux, J. P. Hill, and J. Van Den Brink, *Reviews of Modern Physics* **83**, 705 (2011).

Appendix A: Raw data and analysis for the electronic Green's function

In this section, we provide the full data for $\mathcal{L}_k(t)$ and $|\mathcal{L}_k(\omega)|^2$ obtained via momentum selective linear response applied on SSH model. While the data in the bottom row is shown in Fig. 2 as false color plots, here we provide line plots of the same data for clarity. For each k and δ we collected 3 data sets with 8,000 shots each, yielding 24,000 shots total per curve. As discussed in the main text, $\mu = 5$, $V_{nn} = 1$ and the amplitude of the signal $\eta\Delta t = 0.04$. While obtaining the data we incorporated dynamical decoupling and Pauli twirling as implemented in the *qiskit_research* package, and did not apply any measurement error mitigation method.

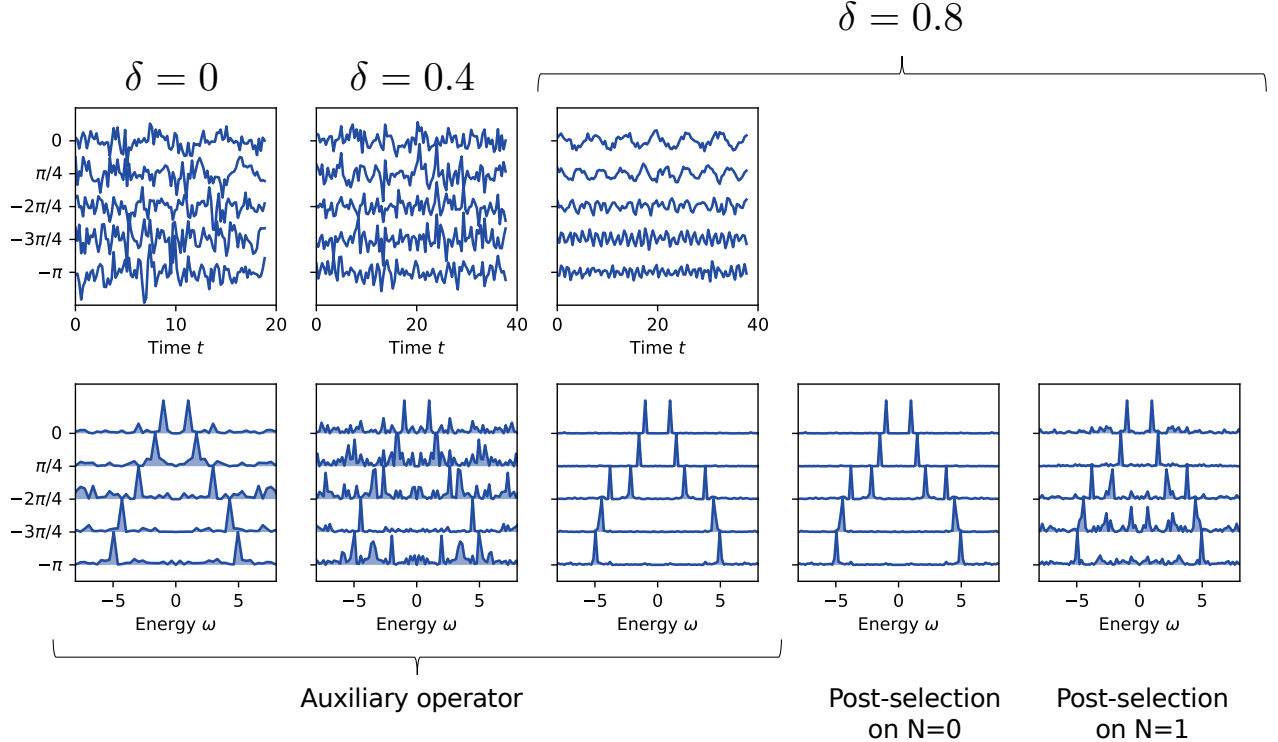


FIG. S1. Data from *ibm_auckland* for the three values of δ presented in the main text, as well as the corresponding $|\mathcal{L}_k(\omega)|^2$. As in the main text, $\mu = 5$ and $V_{nn} = 1$. Note that two copies of the Green's function appear at positive and negative energies (see text for discussion).

Appendix B: Raw data and analysis for the comparison of momentum-selective linear response, real space linear response, and Hadamard test

In order to make a comparison between the linear response method in real and momentum space as well as the Hadamard test method, we performed noisy simulations for each. We constructed a noise model by adding adjustable quantum errors to single and multi qubits gates. The model mainly depends on adding depolarizing quantum channels that mainly decohere qubits; the decoherence is either a result of phase flip or a bit flip or both. We added a fixed single-qubit depolarizing error with a 0.1% rate and a 2-qubit depolarizing error once with a 10% rate and once with a 20% rate. In performing the calculations, we have forced the noisy simulator to respect the linear connectivity found on IBM quantum computers.

The results of the simulations, which are $\mathcal{L}_k(t)$ for the momentum-selective linear response and $\mathcal{L}(r, t)$ for the others, are shown in Fig. S2. The latter two are Fourier transformed to $\mathcal{L}_k(\omega)$ as well, and all three are further transformed to $|\mathcal{L}_k(\omega)|$. As discussed in the main text, and as is clear from the both the line and false-color plots of $|\mathcal{L}_k(\omega)|$, the momentum-selective linear response method outperforms the other two in terms of signal to noise ratio.

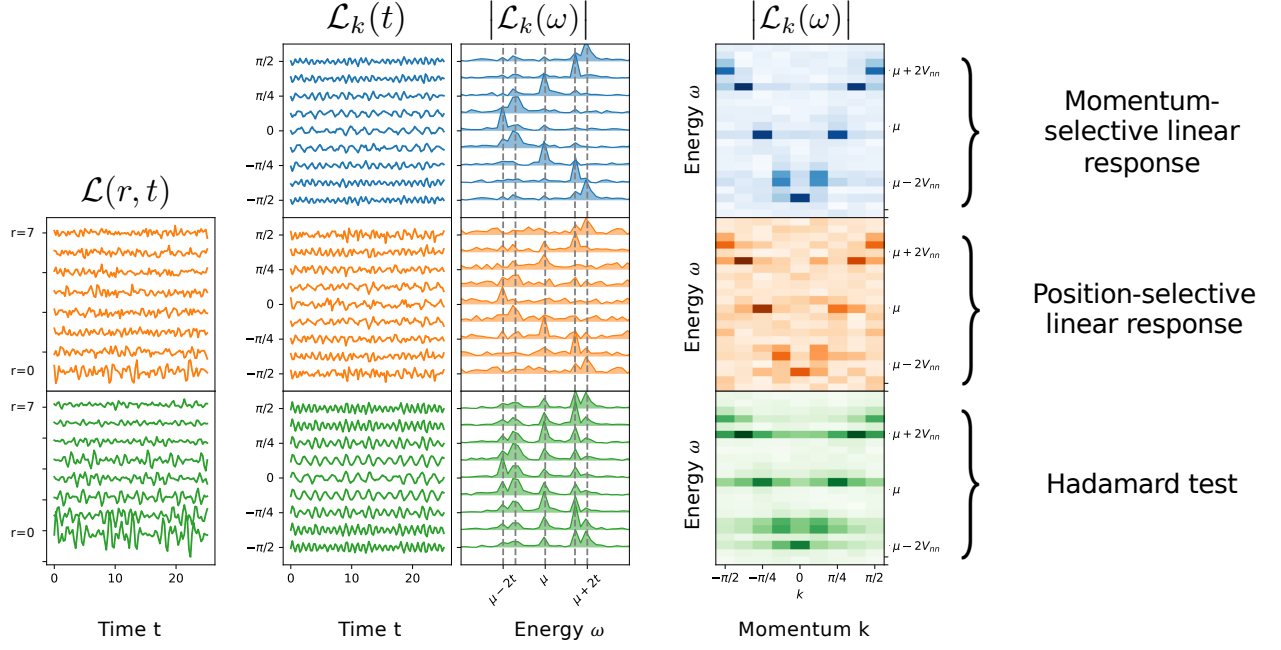


FIG. S2. **Left:** Noisy simulator data of $\mathcal{L}(r, t)$. Note that the momentum-selective method avoids this step. **Center:** momentum-space Green's function as a function of time t or frequency ω . **Right:** false-color plot of $|\mathcal{L}_k(\omega)|$.

Appendix C: Derivation for obtaining $G^>$ and $G^<$ via post-selection

1. Post selection for a particle conserving Hamiltonian for an N -particle initial state

We will demonstrate that the lesser (occupied) and greater (unoccupied) Green's functions can be directly obtained from the measurements by post-selecting on the particle number. In order to do so, we will recast the circuit calculation in fermionic language. Starting from an N -particle state $|\Psi\rangle$, we apply the momentum creation operator $\mathcal{K} = \exp(-i2\eta \sum_m \alpha_m \tilde{X}_m)$ where $\tilde{X}_m = Z_1 \dots Z_{m-1} X_m$ which is equal to $(1/2)(c_m + c_m^\dagger)$ after a Jordan Wigner transformation, to find (to first order in η),

$$\mathcal{K} |\Psi\rangle \approx |\Psi\rangle - i\eta \alpha_m c_m |\Psi\rangle - i\eta \alpha_m c_m^\dagger |\Psi\rangle. \quad (\text{C1})$$

Moreover, for notational clarity we have suppressed internal sums over m by using Einstein summation convention. We next apply the time evolution operator \mathcal{U} , and since we will be measuring the 1st qubit in the X basis, we rotate it by about y ,

$$R_{1y}(\pi/4) = \frac{1}{\sqrt{2}} (1 + c_1^\dagger - c_1). \quad (\text{C2})$$

Applying this to Eq. (C1), we find

$$\begin{aligned} |\Phi^y\rangle := R_{1y}(\pi/4)\mathcal{U}\mathcal{K} |\Psi\rangle &= \frac{1}{\sqrt{2}} \left(\mathcal{U} - i\eta \alpha_m \mathcal{U} c_m - i\eta \alpha_m \mathcal{U} c_m^\dagger \right) |\Psi\rangle \\ &+ \frac{1}{\sqrt{2}} \left(c_1^\dagger \mathcal{U} - i\eta \alpha_m c_1^\dagger \mathcal{U} c_m - i\eta \alpha_m c_1^\dagger \mathcal{U} c_m^\dagger \right) |\Psi\rangle \\ &- \frac{1}{\sqrt{2}} \left(c_1 \mathcal{U} - i\eta \alpha_m c_1 \mathcal{U} c_m - i\eta \alpha_m c_1 \mathcal{U} c_m^\dagger \right) |\Psi\rangle. \end{aligned} \quad (\text{C3})$$

At this point, we can read off the particle number for each term. Since $|\Psi\rangle$ has N particles and the Hamiltonian is particle conserving, counting the number of annihilation and creation operators we see that the resulting state is a

superposition of $N - 2, N - 1, N, N + 1$ and $N + 2$ particle states. These states are

$$\begin{aligned}
|\Phi_{N-2}^y\rangle &= i \frac{\eta}{\sqrt{2}} \alpha_m c_1 \mathcal{U} c_m |\Psi\rangle, \\
|\Phi_{N-1}^y\rangle &= \frac{1}{\sqrt{2}} \left(-c_1 \mathcal{U} - i\eta \alpha_m \mathcal{U} c_m \right) |\Psi\rangle, \\
|\Phi_N^y\rangle &= \frac{1}{\sqrt{2}} \left(\mathcal{U} + i\eta \alpha_m c_1 \mathcal{U} c_m^\dagger - i\eta \alpha_m c_1^\dagger \mathcal{U} c_m \right) |\Psi\rangle, \\
|\Phi_{N+1}^y\rangle &= \frac{1}{\sqrt{2}} \left(c_1^\dagger \mathcal{U} - i\eta \alpha_m \mathcal{U} c_m^\dagger \right) |\Psi\rangle, \\
|\Phi_{N+2}^y\rangle &= -i \frac{\eta}{\sqrt{2}} \alpha_m c_1^\dagger \mathcal{U} c_m^\dagger |\Psi\rangle.
\end{aligned} \tag{C4}$$

We will be measuring expectation values with these states. It will be mainly their norms and expectation value of $c_1^\dagger c_1$ which can be obtained via Z_1 measurement. Observing that $|\Phi_{N\pm 2}\rangle \sim \eta$, they will not contribute up to linear order in η . Independent quantities to linear order in η are

$$\begin{aligned}
\langle \Phi_{N-1}^y | \Phi_{N-1}^y \rangle &= \frac{1}{2} \langle n_1(t) \rangle + \frac{i\eta \alpha_m}{2} \left(\langle c_1^\dagger(t) c_m \rangle - \langle c_m^\dagger c_1(t) \rangle \right) = \frac{1}{2} \langle n_1(t) \rangle - \eta \alpha_m \text{Re } G_{1m}^<(t) \\
\langle \Phi_{N+1}^y | \Phi_{N+1}^y \rangle &= \frac{1}{2} - \frac{1}{2} \langle n_1(t) \rangle + \frac{i\eta \alpha_m}{2} \left(\langle c_m c_1^\dagger(t) \rangle - \langle c_1(t) c_m^\dagger \rangle \right) = \frac{1}{2} - \frac{1}{2} \langle n_1(t) \rangle + \eta \alpha_m \text{Re } G_{1m}^>(t) \\
\langle \Phi_N^y | c_1^\dagger c_1 | \Phi_N^y \rangle &= \frac{1}{2} \langle n_1(t) \rangle + \frac{i\eta \alpha_m}{2} \left(\langle c_m^\dagger c_1(t) \rangle - \langle c_1^\dagger(t) c_m \rangle \right) = \frac{1}{2} \langle n_1(t) \rangle + \eta \alpha_m \text{Re } G_{1m}^<(t)
\end{aligned} \tag{C5}$$

This leads to first two equations of Eq.(12). Instead, if we apply a rotation around x we get:

$$R_{1x}(\pi/4) = \frac{1}{\sqrt{2}} \left(1 + ic_1^\dagger + ic_1 \right), \tag{C6}$$

then

$$\begin{aligned}
|\Phi^x\rangle := R_{1x}(\pi/4) \mathcal{U} \mathcal{K} |\Psi\rangle &= \frac{1}{\sqrt{2}} \left(\mathcal{U} - i\eta \alpha_m \mathcal{U} c_m - i\eta \alpha_m \mathcal{U} c_m^\dagger \right) |\Psi\rangle \\
&+ \frac{i}{\sqrt{2}} \left(c_1^\dagger \mathcal{U} - i\eta \alpha_m c_1^\dagger \mathcal{U} c_m - i\eta \alpha_m c_1^\dagger \mathcal{U} c_m^\dagger \right) |\Psi\rangle \\
&+ \frac{i}{\sqrt{2}} \left(c_1 \mathcal{U} - i\eta \alpha_m c_1 \mathcal{U} c_m - i\eta \alpha_m c_1 \mathcal{U} c_m^\dagger \right) |\Psi\rangle.
\end{aligned} \tag{C7}$$

Then, the components with different particle number are

$$|\Phi_{N-2}^x\rangle = \frac{\eta}{\sqrt{2}} \alpha_m c_1 \mathcal{U} c_m |\Psi\rangle, \tag{C8a}$$

$$|\Phi_{N-1}^x\rangle = \frac{1}{\sqrt{2}} \left(ic_1 \mathcal{U} - i\eta \alpha_m \mathcal{U} c_m \right) |\Psi\rangle, \tag{C8b}$$

$$|\Phi_N^x\rangle = \frac{1}{\sqrt{2}} \left(\mathcal{U} + \eta \alpha_m c_1 \mathcal{U} c_m^\dagger + \eta \alpha_m c_1^\dagger \mathcal{U} c_m \right) |\Psi\rangle, \tag{C8c}$$

$$|\Phi_{N+1}^x\rangle = \frac{1}{\sqrt{2}} \left(ic_1^\dagger \mathcal{U} - i\eta \alpha_m \mathcal{U} c_m^\dagger \right) |\Psi\rangle, \tag{C8d}$$

$$|\Phi_{N+2}^x\rangle = \frac{\eta}{\sqrt{2}} \alpha_m c_1^\dagger \mathcal{U} c_m^\dagger |\Psi\rangle. \tag{C8e}$$

To linear order in η , independent quantities that can be derived from norms and the expectation value of Z_1 are

$$\begin{aligned}
\langle \Phi_{N-1}^x | \Phi_{N-1}^x \rangle &= \frac{1}{2} \langle n_1(t) \rangle - \frac{\eta \alpha_m}{2} \left(\langle c_1^\dagger(t) c_m \rangle + \langle c_m^\dagger c_1(t) \rangle \right) \\
&= \frac{1}{2} \langle n_1(t) \rangle - \eta \alpha_m \text{Im} G_{1m}^<(t) \\
\langle \Phi_{N+1}^x | \Phi_{N+1}^x \rangle &= \frac{1}{2} - \frac{1}{2} \langle n_1(t) \rangle - \frac{\eta \alpha_m}{2} \left(\langle c_m c_1^\dagger(t) \rangle + \langle c_1(t) c_m^\dagger \rangle \right) \\
&= \frac{1}{2} - \frac{1}{2} \langle n_1(t) \rangle + \eta \alpha_m \text{Im} G_{1m}^>(t) \\
\langle \Phi_N^x | c_1^\dagger c_1 | \Phi_N^x \rangle &= \frac{1}{2} \langle n_1(t) \rangle + \frac{\eta \alpha_m}{2} \left(\langle c_m^\dagger c_1(t) \rangle + \langle c_1^\dagger(t) c_m \rangle \right) \\
&= \frac{1}{2} \langle n_1(t) \rangle + \eta \alpha_m \text{Im} G_{1m}^<(t)
\end{aligned}$$

These can be linearly combined to obtain the final two equations of Eq. (12) in the main text, and shows that retarded, lesser and greater fermionic Green's functions can be calculated via post selection.

2. Post selection for SSH model for 0-particle initial state

In this case our calculation simplifies drastically, since we cannot annihilate a particle from a 0-particle state, and thus the only contribution will come from 0, 1 and 2 particle states:

$$\begin{aligned}
|\Phi_0^y\rangle &= \frac{1}{\sqrt{2}} \left(\mathcal{U} + i\eta \alpha_m c_1 \mathcal{U} c_m^\dagger - i\eta \alpha_m c_1^\dagger \mathcal{U} c_m \right) |0\rangle \\
&= \frac{1}{\sqrt{2}} \left(\mathcal{U} + i\eta \alpha_m c_1 \mathcal{U} c_m^\dagger \right) |0\rangle, \\
|\Phi_1^y\rangle &= \frac{1}{\sqrt{2}} \left(c_1^\dagger \mathcal{U} - i\eta \alpha_m \mathcal{U} c_m^\dagger \right) |0\rangle, \\
|\Phi_2^y\rangle &= -i \frac{\eta}{\sqrt{2}} \alpha_m c_1^\dagger \mathcal{U} c_m^\dagger |0\rangle. \tag{C9}
\end{aligned}$$

The norm of the 2-particle contribution is $O(\eta^2)$ and is neglected. The norms of 0- and 1-particle contributions are

$$\begin{aligned}
\langle \Phi_0^x | \Phi_0^y \rangle &= \frac{1}{2} - \eta \alpha_m \text{Re} G_{1m}^>(t), \\
\langle \Phi_1^x | \Phi_1^y \rangle &= \frac{1}{2} + \eta \alpha_m \text{Re} G_{1m}^>(t).
\end{aligned}$$

Because the lesser Green's function of the 0-particle state $|0\rangle$ is zero, we can replace the greater Green's functions with the retarded ones:

$$\begin{aligned}
\langle \Phi_0^x | \Phi_0^y \rangle &= \frac{1}{2} - \eta \alpha_m \text{Re} G_{1m}^R(t), \\
\langle \Phi_1^x | \Phi_1^y \rangle &= \frac{1}{2} + \eta \alpha_m \text{Re} G_{1m}^R(t),
\end{aligned}$$

and therefore these partial norms contain information about the single-particle energy spectrum.

Appendix D: Quantum circuit for the SSH Model Green's function

The circuit in Fig. 2b mainly consists of three parts: the applied field $\mathbf{B}h(t)$, the time evolution and the measurement of \mathbf{A} . Here we will discuss how to use the parity operator as an auxiliary to measure fermionic Green's functions.

1. Measurement of $\text{Re } G_k(\omega)$

In this work, we measure the following quantity for SSH model on no particle state $|0\rangle$

$$\mathcal{L}_k(t) = -i \langle 0 | \left[X_0(t), \sum_r \cos(kr) X_r \right] | 0 \rangle. \quad (\text{D1})$$

We will slowly change this into an expression given in terms of Green's functions, and show that $\mathcal{L}_k(t)$ contains information about the one particle spectral weight.

First observe that $\tilde{X}_r |0\rangle = X_r |0\rangle$. In addition, for $P = Z_0 Z_1 \dots Z_n$ we have $P |0\rangle = |0\rangle$, therefore

$$\begin{aligned} \mathcal{L}_k(t) &= -i \langle 0 | \left[X_0(t), \sum_r \cos(kr) \tilde{X}_r \right] P | 0 \rangle \\ &= i \langle 0 | \left\{ X_0(t) P, \sum_r \cos(kr) \tilde{X}_r \right\} | 0 \rangle \\ &= i \langle 0 | \left\{ X_0(t) P(t), \sum_r \cos(kr) \tilde{X}_r \right\} | 0 \rangle. \end{aligned} \quad (\text{D2})$$

On the last line, we have used $P(t) = P$. Eq. D2 is essentially the auxiliary operator method given in the manuscript applied in reverse way to transform commutator into anti-commutator. Now $X_0 P = -i \tilde{Y}_0 Z_1 \dots Z_{n-1}$, and $Z_1 \dots Z_{n-1} |0\rangle = |0\rangle$. In addition, $\tilde{Y}_0 = Y_0$, then

$$\mathcal{L}_k(t) = \langle 0 | \left\{ \tilde{Y}_0(t), \sum_r \cos(kr) \tilde{X}_r \right\} | 0 \rangle. \quad (\text{D3})$$

Applying the Jordan-Wigner transformation to get the Fermionic operators back, let us plug in $\tilde{X}_r = c_r + c_r^\dagger$ and $\tilde{Y}_0 = i(c_0^\dagger - c_0)$:

$$\begin{aligned} \sum_r \cos(kr) \tilde{X}_r &= \frac{1}{2} \sum_r (e^{ikr} + e^{-ikr}) (c_r + c_r^\dagger) = \frac{\sqrt{n}}{2} (c_k + c_{-k} + c_k^\dagger + c_{-k}^\dagger) \\ \tilde{Y}_0 &= i(c_0^\dagger - c_0) = \frac{i}{\sqrt{n}} \sum_q (c_q^\dagger - c_q). \end{aligned} \quad (\text{D4})$$

With these, we obtain

$$\begin{aligned} \mathcal{L}_k(t) &= -\frac{i}{2} \langle 0 | \left\{ \sum_q (c_q(t) - c_q^\dagger(t)), (c_k + c_{-k} + c_k^\dagger + c_{-k}^\dagger) \right\} | 0 \rangle. \\ &= -\frac{i}{2} \sum_q \left(\langle 0 | \{c_q(t), c_k^\dagger + c_{-k}^\dagger\} | 0 \rangle - \langle 0 | \{c_q^\dagger(t), c_k + c_{-k}\} | 0 \rangle \right). \end{aligned} \quad (\text{D5})$$

The sum can be handled directly because momentum is conserved due to translational invariance of the SSH model, then the creation/annihilation operators anticommute when momentum values are not matched. Since we assume $t > 0$, we can plug in $\theta(t) = 1$ in the definition of $G_k^R(t)$, and then obtain

$$\begin{aligned} \mathcal{L}_k(t) &= \frac{1}{2} (G_k^R(t) + G_{-k}^R(t) + G_k^R(t)^* + G_{-k}^R(t)^*) \\ &= \text{Re}(G_k^R(t) + G_{-k}^R(t)). \end{aligned} \quad (\text{D6})$$

The SSH model is symmetric under spatial reflection, thus $G_k^R = G_{-k}^R$ and we get

$$\mathcal{L}_k(t) = 2 \text{Re } G_k^R(t) \quad (\text{D7})$$

Let us look at this in the frequency basis:

$$\begin{aligned} \mathcal{L}_k(\omega) &= \int dt \mathcal{L}_k(t) e^{i\omega t} \\ &= 2 \int dt \text{Re } G_k^R(t) e^{i\omega t} \\ &= \int dt (G_k^R(t) + G_k^R(t)^*) e^{i\omega t} \\ &= G_k^R(\omega) + G_k^R(-\omega)^* \end{aligned} \quad (\text{D8})$$

Then we get

$$\begin{aligned}\text{Im } \mathcal{L}_k(\omega) &= \text{Im } G_k^R(\omega) - \text{Im } G_k^R(-\omega), \\ \text{Re } \mathcal{L}_k(\omega) &= \text{Re } G_k^R(\omega) + \text{Re } G_k^R(-\omega),\end{aligned}\tag{D9}$$

which means that choosing \mathbf{A} and \mathbf{B} as given in the beginning of this subsection, we can get single particle spectral weight.

Both momentum selective and position selective methods can be used to measure $\mathcal{L}_k(t)$. The momentum selective method is to excite the state $|0\rangle$ with $\mathbf{B} = \sum_r \cos(kr)X_r$ and measuring X_0 after time evolution, which can measure $\mathcal{L}_k(t)$ with one circuit. The position selective method is to measure X_0 after exciting the state with $\mathbf{B} = X_r$ and time evolving for all $r = 1, 2, \dots, n$ values.

For the data shown in Figs. 2 and 3, we only measure $\mathcal{L}_k(t)$ in linear response methods with momentum and position selectivity, to run fewer circuits. The plots show $|\mathcal{L}_k(\omega)|^2$, which is related to the retarded Green's function as

$$\begin{aligned}|\mathcal{L}_k(\omega)|^2 &= \left(G_k^R(\omega) + G_k^R(-\omega)^*\right) \left(G_k^R(\omega)^* + G_k^R(-\omega)\right), \\ &= |G_k^R(\omega)|^2 + |G_k^R(-\omega)|^2 + 2\text{Re}\left(G_k^R(\omega)G_k^R(-\omega)^*\right).\end{aligned}\tag{D10}$$

Because $G_k^R(\omega)$ is strongly peaked near the single-particle excitation energy, the interference term is negligible compared to the absolute squares of the terms $G_k^R(\omega)$ and $G_k^R(-\omega)$. Therefore $|\mathcal{L}_k(\omega)|^2$ contains $|G_k^R(\omega)|^2$ and its mirror image in the plots. Due to our chemical potential choice $\mu = 5$, in the positive frequencies, we only see one of these images, which gives us the information about the single particle spectrum. Fig. S3 illustrates this point by showing that $|\mathcal{L}_k(\omega)|$ tracks the quasi-particle peaks in $|G_k^R(\omega)|$ and $\text{Im } G_k^R(\omega)$. In the figure, we compare the real part, imaginary part and absolute value of $G_k^R(\omega)$

$$G_k^R(\omega) = \frac{1}{\omega - \omega_k + i\epsilon},\tag{D11}$$

where $\epsilon = 0.1$, and we picked $\omega_k = 5$. As it can be seen on panel **a**, $|G^R(\omega)|$ is peaked at ω_k just as $\text{Im } G_k^R(\omega)$, with a slightly broader peak. Panel **b** shows that $|\mathcal{L}_k(\omega)|$ is small except at $\omega = \pm\omega_k$ energies, which are the peaks of $|G^R(\omega)|$ and $|G^R(-\omega)|$. This provides an illustration of the fact that the interference term in Eq. D10 is indeed negligible.

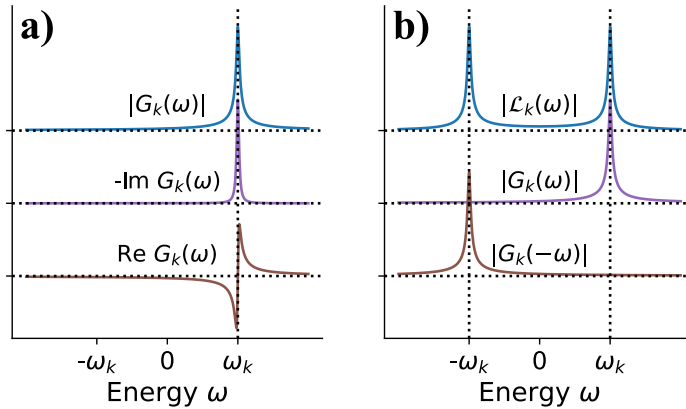


FIG. S3. Panel **a** illustrates that $|G_k^R(\omega)|$ has the same spectral behaviour as $\text{Im } G_k^R(\omega)$, and therefore carries information about the single particle spectral weight. Panel **b** illustrates that this spectral information can be extracted from $|\mathcal{L}_k(\omega)|$ since it has two distinctive peaks, one coming from $|G_k^R(\omega)|$, the other from $|G_k^R(-\omega)|$.

2. Time Evolution Circuit

The SSH model is a free fermionic model and thus its time evolution can be compressed into a fixed depth circuit with $O(n^2)$ CNOTs and $O(n)$ depth, where n is the system size, via the algebraic compression method given in [39, 40].

The method is limited to free fermionic systems in 1D — here we use a generalization to 1D periodic systems, which will be detailed in a forthcoming publication.

For completeness, we will summarize the method for the open 1-D chain. The method relies on a structure called a “block”, and is given as the following for free fermionic models (after performing the Jordan-Wigner transformation):

$$B_i(\vec{\theta}) \equiv e^{-i\theta_1 Z_i} e^{-i\theta_2 Z_{i+1}} e^{-i\theta_3 X_i X_{i+1}} e^{-i\theta_4 Y_i Y_{i+1}} e^{-i\theta_5 Z_i} e^{-i\theta_6 Z_{i+1}}. \quad (\text{D12})$$

We represent it as the diagram shown in Fig. S4. In Ref. 39 it is proven that $B_i(\vec{\theta})$ satisfies the following properties:

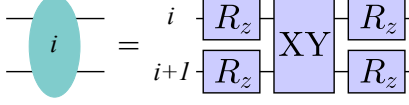


FIG. S4. Block given in (D12) represented as a 2 qubit gate. XY indicates a rotation about XX followed by YY [39, 40]. R_z , and the XX and YY rotations have independent rotation angles.

1. **Fusion:** for any set of parameters $\vec{\alpha}$ and $\vec{\beta}$, there exists an \vec{a} such that

$$B_i(\vec{\alpha}) B_i(\vec{\beta}) = B_i(\vec{a}), \quad (\text{D13})$$

2. **Commutation:** for any set of parameters $\vec{\alpha}$ and $\vec{\beta}$, we have

$$B_i(\vec{\alpha}) B_j(\vec{\beta}) = B_j(\vec{\beta}) B_i(\vec{\alpha}), \quad |i - j| > 1, \quad (\text{D14})$$

3. **Turnover:** for any set of parameters $\vec{\alpha}$, $\vec{\beta}$ and $\vec{\gamma}$ there exist \vec{a} , \vec{b} and \vec{c} such that

$$B_i(\vec{\alpha}) B_{i+1}(\vec{\beta}) B_i(\vec{\gamma}) = B_{i+1}(\vec{a}) B_i(\vec{b}) B_{i+1}(\vec{c}). \quad (\text{D15})$$

These properties can be exploited to build the triangle structure shown in Fig. S5 a, which can absorb any additional block by simple parameter changes. Calculation of the parameters can be done directly via linear algebra operations without any variational calculation, the details of which are given in [40].

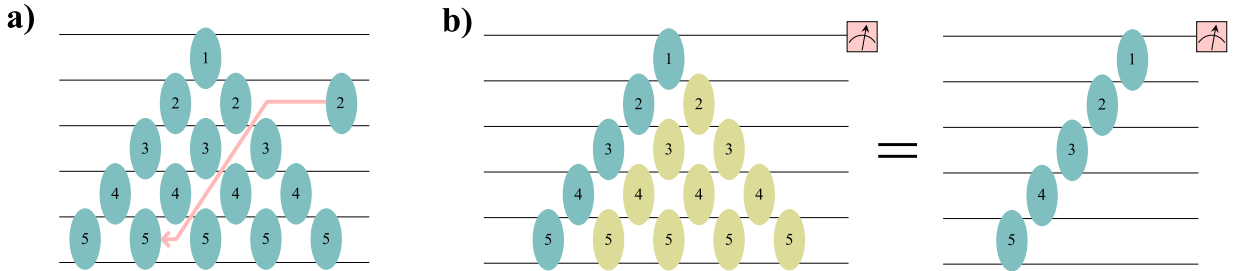


FIG. S5. Panel a demonstrates the triangle structure and how it can absorb a block. Block with index 2 goes down with a series of turnover operations, and ends up merging the block at the end of the arrow. Panel b demonstrates the additional simplification due to measurement. Blocks with gold color has no effect on the measurement on the 0th qubit, and therefore can be discarded, reducing the CNOT count from $O(n^2)$ to $O(n)$.

For the momentum selective case we only need to measure the 0th site, and thus the information on the other qubits are not relevant. As shown in Fig. S5 b, because the measurement is on qubit 0, blocks that do not affect qubit zero can be pushed after the measurement, and therefore can be ignored. Although post-selection requires measurement of all qubits, this simplification can still be done simply because the only information used from the other qubits is the particle number, and the TFX blocks do not change the particle number.

The triangle structure CNOT count is $n(n-1)/2$, which is 28 for the $n = 8$ calculations presented in the main text. After this measurement simplification, the CNOT count decreases to $2(n-1)$, or 14 for our calculations.

Appendix E: Hardware Calibration Details

The results from the quantum computer shown in Fig. 2 were run on *ibmq_auckland* via the IBM Quantum Experience. Calibration information for the two dates we collected data are shown in Tables S1 and S2 and were obtained from the Qiskit API [42].

Qubits	T1 (μs)	T2 (μs)	readout error (%)	CNOT connection	CNOT error (%)
13	140	27.6	0.56	13-12	0.536
12	256	232	1.84	12-10	0.835
10	225	49.2	0.91	10-7	0.544
7	130	218	0.92	7-4	0.933
4	176	164	1.85	4-1	1.08
1	52.7	135	0.95	1-2	0.594
2	173	177	1.61	2-3	0.516
3	104	67.6	1.55		

TABLE S1. Calibration data for *ibmq_auckland* on September 19th, 2022.

Qubits	T1 (μs)	T2 (μs)	readout error (%)	CNOT connection	CNOT error (%)
0	372	420	0.80	0-1	0.504
1	398	285	1.02	1-2	0.763
2	528	413	0.86	2-3	0.382
3	365	131	1.29	3-5	0.340
5	253	371	21.7	5-8	0.428
8	353	109	1.67	8-11	0.371
11	146	309	1.10	11-14	0.441
14	468	129	22.9		

TABLE S2. Calibration data for *ibmq_auckland* on September 30th, 2022.